

# Effects of Sideslip on the Aerodynamics of Low-Aspect-Ratio Low-Reynolds-Number Wings

Matt Shields\* and Kamran Mohseni†  
University of Florida, Gainesville, Florida 32611-6250

DOI: 10.2514/1.J051151

The growing interest in micro aerial vehicles has brought attention to the need for an improved understanding of the aerodynamics of low-aspect-ratio wings at low Reynolds numbers. In this study, flat plate wings with rectangular and tapered planforms were fabricated with aspect ratios of 0.75, 1, 1.5, and 3, and the aerodynamic loading was measured at Reynolds numbers between  $5 \times 10^4$  and  $1 \times 10^5$ . Surface tuft visualization was used to observe the interactions between the tip vortices and the leading-edge vortex. The tests were initially conducted at a sideslip angle of  $0^\circ$  and were then repeated for  $\beta = 10, 20,$  and  $35^\circ$  with and without winglets. Measurements made with a six-component force balance showed that a decrease in aspect ratio caused an increase in  $\alpha_{\text{stall}}$  and  $C_{L_{\text{max}}}$  due to the nonlinear lift induced by the interacting flow on the upper wing surface. In addition, the detachment of tip vortices after stall leads to a sudden decrease in drag coefficient as the magnitude of the induced drag drops significantly. At increasing sideslip angles, the effects of the crossflow still contribute to an increase in lift but significantly reduce the pitching moment about the quarter-chord, thus decreasing the wing's ability to recover from angle-of-attack perturbations. These results show that, while the effects of tip vortices and the leading-edge vortex complicate the flowfield around a low-aspect-ratio wing, particularly at increased sideslip angles, their impact tends to improve the aerodynamic performance.

## Nomenclature

$b$	=	wingspan, in.
$C_D$	=	drag coefficient
$C_L$	=	lift coefficient
$C_{L_{\text{max}}}$	=	maximum lift coefficient (at stall)
$C_M$	=	pitching moment coefficient about quarter-chord
$C_{M,\alpha}$	=	pitch stiffness derivative
$c_{\text{root}}$	=	root chord, in.
$c_{\text{tip}}$	=	tip chord, in.
$f$	=	vortex shedding frequency, Hz
$S$	=	wing planform area, ft <sup>2</sup>
$St$	=	Strouhal number,
$Re$	=	Reynolds number,
$U_0$	=	freestream velocity, ft/s
$\alpha$	=	angle of attack, $^\circ$
$\alpha_{\text{stall}}$	=	stall angle of attack, $^\circ$
$\beta$	=	sideslip angle, $^\circ$
$\lambda$	=	taper ratio

## I. Introduction

IN THE past decade, a growing interest has developed in the field of low-Reynolds-number low-aspect-ratio (LAR) aerodynamics with the goal of aiding the design of micro aerial vehicles (MAVs). These aircraft, used for various remote sensing operations, are smaller than 6 in. (15 cm) in all dimensions and typically weigh less than 5 oz. (150 g) [1]. Several different organizations have developed a diverse set of MAVs for a variety of applications, all with varying dimensions, planform geometries, duration requirements, and control surfaces [2–6]. Although many

different designs have been proven to be acceptable sensor platforms, there are inherent difficulties associated with the design of these vehicles due to the complex flow regime of MAV flight. When designing a small wing, the maximum lifting performance can be achieved with an aspect ratio (AR) on the order of unity. The resulting short wingspan allows the effects of tip vortices to propagate over a significant portion of the wing, increasing induced drag and nonlinear lift at high angles of attack [7,8]. In addition, the range of Reynolds numbers usually associated with MAV flight ( $5 \times 10^4$ – $2 \times 10^5$ ) is characterized by the development of a laminar separation bubble on the top surface of the wing that contributes to the stalling characteristics of the wing and the unsteady flow developing behind the bubble [9,10]. Finally, the leading-edge separated shear layer rollup on many MAV wings leads to the development of the leading-edge vortex (LEV), which can create numerous unsteady and adverse flow effects such as vortex bursting on the top surface of the wing [11,12]. These phenomena make it difficult to accurately predict the aerodynamic performance of LAR low-Reynolds-number fliers, particularly at high angles of attack; hence, an experimental investigation is necessary to assist in the development of future MAVs.

There are few studies available on the effects of low-Reynolds-number flows on the aerodynamic loading of small wings; perhaps the most complete study available is the excellent work done by Torres and Mueller [8] investigating predominantly the lifting behavior associated with thin rectangular, Zimmerman, inverse Zimmerman, and elliptical wings at Reynolds numbers between  $7 \times 10^4$  and  $2 \times 10^5$ . The authors were able to quantify the nonlinear lifting performance and compare the wing efficiency at different ARs and angles of attack. The goal of this paper is to further investigate similar geometries with the additional consideration of varying sideslip angles, taper ratios, and winglet configurations. Flight testing at the University of Colorado has indicated that MAVs are susceptible to lateral gust perturbations that can sometimes initiate unrecoverable instability modes [13–16], justifying the importance of measuring the effects of sideslip on aerodynamic performance. Wind-tunnel testing on flat plates with different configurations and ARs between 0.75 and 3 was used to investigate the aerodynamic behavior of LAR wings at low Reynolds numbers between  $5 \times 10^4$  and  $1 \times 10^5$ .

Received 31 December 2010; revision received 10 June 2011; accepted for publication 8 August 2011. Copyright © 2011 by the American Institute of Aeronautics and Astronautics, Inc. All rights reserved. Copies of this paper may be made for personal or internal use, on condition that the copier pay the \$10.00 per-copy fee to the Copyright Clearance Center, Inc., 222 Rosewood Drive, Danvers, MA 01923; include the code 0001-1452/12 and \$10.00 in correspondence with the CCC.

\*Graduate Research Assistant, Department of Mechanical and Aerospace Engineering. Student Member AIAA.

†William P. Bushnell Endowed Chair in Mechanical and Aerospace Engineering Department and Electrical and Computer Engineering Department. Associate Fellow AIAA.

## II. Experimental Setup

### A. Wind Tunnel

All tests were conducted for this research using the prototunnel at the University of Colorado Wind and Gust Characterization Laboratory and at the Particle Engineering Research Center laboratory at the University of Florida. This low-turbulence open-circuit closed-jet wind tunnel has a  $14 \times 14$  in. test section with an 8.5:1 contraction ratio. An aluminum honeycomb screen with 0.25 in. apertures is used as a flow straightener with a fine mesh screen immediately downstream that helps to reduce the freestream turbulence intensity in the tunnel to 0.2% in the range of velocities tested (20–65 ft/s). The test section is 5 ft long with the test models mounted 4 ft downstream of the contraction cone exit.

### B. Model Positioning System

The objective of this research is to measure aerodynamic effects at a wide variety of flight angles. Many low-Reynolds-number tunnels use an external force balance to test flat plate geometries mounted to endplates near the walls of the test section, enabling comparison with two-dimensional results. This has the disadvantage of effectively blocking the tip vortices from propagating over the wingtips, which is the main phenomena being investigated. Torres and Mueller used an internal force balance mounted to the trailing edge of the test model, allowing full development of the tip vortices [8]. Some tunnels employ a dynamic positioning system to induce pitching and plunging motions of a test model [17]. The prototunnel is outfitted with a model positioning system (MPS), which was designed and built by the authors to increase the available degrees of freedom that can be tested while maintaining the effects of tip vortices.

The MPS (shown in Fig. 1) is mounted under the test section and uses a series of three Danaher Motion Nema-23 stepper motors for roll, pitch, and yaw actuation and a Haydon-Kerk 57000 series noncaptive linear actuator to control the model in a vertical plunge. These motors can rotate the MPS  $\pm 180^\circ$  in roll,  $\pm 40^\circ$  in pitch, and  $\pm 180^\circ$  in yaw, in addition to being able to plunge a total distance of  $\pm 14$  in.. It should be noted that these ranges are the allowable displacements of the MPS itself and do not necessarily reflect the

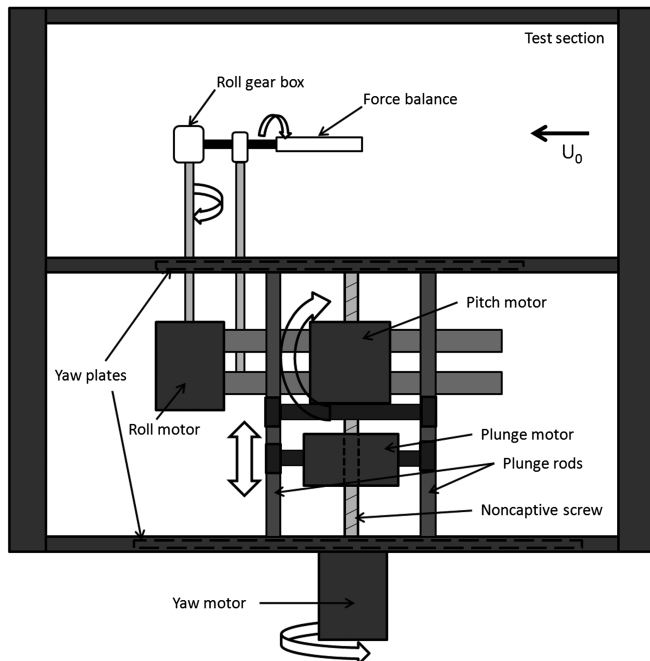
maximum range that can be tested for a specific model. Test models at higher angles can potentially breach the boundary layer of the tunnel or produce forces that overload the balance; thus, some test cases are not taken to the absolute maximum of corresponding MPS axis. Multiple axes can be controlled simultaneously to induce maneuvering flight (i.e., combining roll and pitch to mimic a banked turn) by running LabVIEW software and National Instruments hardware (a PXI-7330 motion controller, a UMI-7774 universal motion interface, and four Pacific Scientific P70530 controllers).

### C. Force Balance and Data Acquisition System

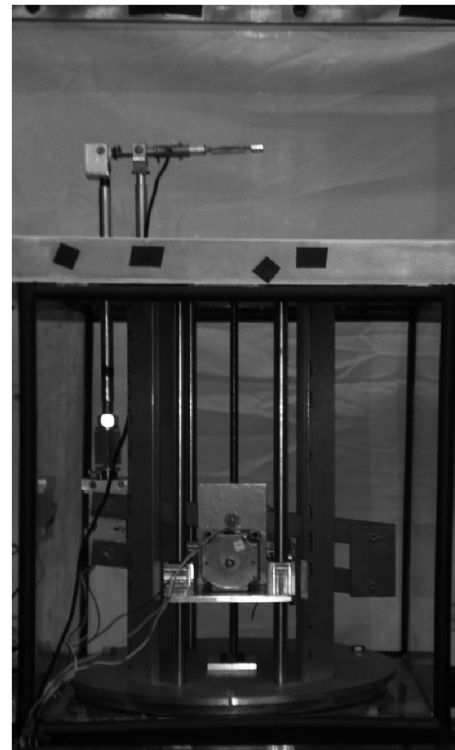
All measurements were conducted using the microloading technology (MLT) force balance, custom built by Modern Machine and Tool Company (MMT) in Norfolk, VA. This six-component internal balance was designed to measure MAV-scale loads with a high accuracy; the specifications for each channel can be found in Table 1. The 24 strain gauges were configured as six full Wheatstone bridges. The data were collected at 10,000 samples for each model position using a National Instruments SCXI-1520 eight-channel strain gauge module at a sampling frequency of 10 kHz with a low-pass Butterworth filter set at 1 kHz and were then converted by a 16-bit A/D converter. Physical loads were then computed from the strain voltages using an iterative technique based upon the AIAA standard for strain gauge measurements [18]. A significant amount of calibration testing was conducted on the balance by both MMT and the authors to validate its performance. A major issue detected with weight measurements was inaccurate axial force (AF) readings at low loadings due to the magnitude of the output voltage being below the usable threshold of the SCXI-1520; an amplification circuit was appended to the AF channel and resulted in less than 1% error in measurements on the order of 0.01 lb (5 g).

### D. Models and Testing Procedure

Flat plate (0% camber) models were manufactured for this investigation in a manner common to other LAR wind-tunnel studies. The plates were machined with a 5:1 elliptically rounded leading edge and had thickness-to-root chord ratios between 2.4 and 5.4%.



a) MPS schematic



b) MPS photo

Fig. 1 MPS mounted under the test section. Block arrows indicate available degrees of freedom that can be actuated by each motor (figure not to scale).

**Table 1** MLT balance maximum loads and errors

Channel	Maximum load	Maximum error, % of full scale load	Typical MAV load ( $\alpha = 30^\circ$ , $\beta = 20^\circ$ , $Re = 10^5$ )
Normal force	3 lb	0.13	0.39 lb
Axial force	2 lb	0.19	0.07 lb
Pitching moment	5 in. · lb	0.12	0.13 in. · lb
Rolling moment	3 in. · lb	0.18	0.12 in. · lb
Yawing moment	3 in. · lb	0.20	0.06 in. · lb
Side force	2 lb	0.14	0.04 in. · lb

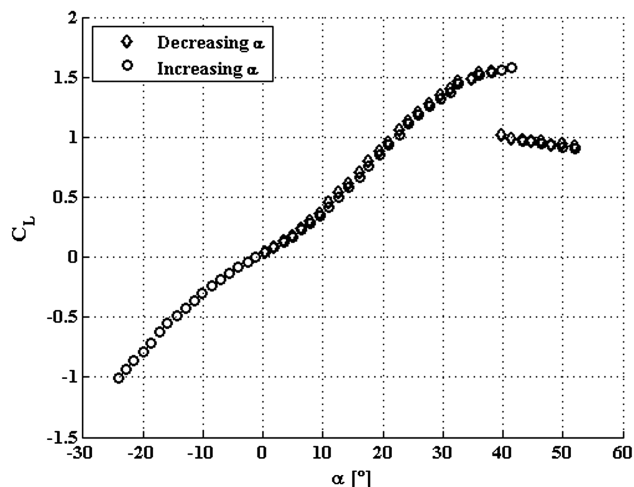
The small dimensions of the prototunnel test section require that the maximum span of a model must be less than 10 in. to ensure that it does not intrude upon the tunnel wall boundary layer. The models were machined from acrylic instead of the more traditional aluminum to reduce the weight that the balance needs to support. The dimensions of the models are listed in Table 2.

Winglets were also machined to investigate the effects of reducing the tip vortex flow on the top surface of the tapered wings. These additions were 1.5 in. high and the same length as the tip chord (1.5, 3, and 4.5 in.). The leading edge was rounded on one side with a 5:2 elliptical geometry and was flat on the other side, allowing it to be mounted flush to the wing. They were attached to the wing in three configurations: entirely above the wing, centered on the wing, and entirely below the wing, as shown in Table 2, in order to determine which geometry had the greatest effect on the aerodynamics. Models were mounted to the MLT balance at their three-quarter-chord using a cylindrical mount attached flush with the bottom surface of the model along the centerline. Although the mount was tapered to reduce drag, it was initially a concern that its 0.5 in. diameter would have a significant impact on the loading; however, trials run with the mount on the top surface and bottom surface of the wing, as well as results with the mount drag subtracted out, produced identical data. Hence, interference from the mount was deemed to be negligible.

As repeatability of results is a vital aspect of wind-tunnel testing, a rigid testing protocol was followed for every trial. The model was mounted to the MLT balance and oriented in the tunnel using a digital protractor. Initial testing indicated that the moment from the aerodynamic loads on the model caused the cantilevered support arm of the MPS to deflect; thus, a Phantom v4.3 high-speed camera was used to noninvasively measure the desired angles for the trial from outside of the test section with the wind running. This reduced the uncertainty in the angle measurement to less than  $0.2^\circ$ . To collect the data, a “zero reference data set” was obtained by sweeping the test

**Table 2** Test model dimensions

AR	$c_{root}$ , in.	$c_{tip}$ , in.	$b$ , in.	$\lambda$	Diagram
<i>Rectangular planform</i>					
0.75	6.67	6.67	5.00	1	
1	6.00	6.00	6.00	1	
1.5	4.00	4.00	6.00	1	
3	3.00	3.00	9.00	1	
<i>Tapered planform</i>					
1	6.00	4.50	6.00	0.75	
1	6.00	3.00	6.00	0.5	
1	6.00	1.50	6.00	0.25	
<i>Winglet configuration (front view)</i>					
1	6.00	4.50	6.00	0.75	
1	6.00	3.00	6.00	0.5	
1	6.00	1.50	6.00	0.25	

**Fig. 2** Hysteresis measurements for a flat plate with  $AR = 1$  at  $Re = 1 \times 10^5$ .

model through the desired angles with the wind off before running the same sweep with the wind on. Comparing the loads at each data point yields the aerodynamic forces and moments while accounting for the weight of the model. Each data run was started at the most negative angle of attack (approximately  $-24^\circ$ ) and finished at the highest positive angle (typically around  $45^\circ$ ), and it was then returned to a zero angle to detect any hysteresis in the data. A small amount was recorded in the form of a  $3^\circ$  decrease in  $\alpha_{stall}$  (for illustrative purposes, a test case with a flat plate of  $AR = 1$  at  $Re = 1 \times 10^5$  is shown in Fig. 2). This indicates that low turbulence level in the test section has a slight effect in causing the laminar boundary layer to separate from the wing at high angles of attack instead of transitioning to turbulence, as reported by Mueller et al. [19]. Finally, another zero reference set was taken to determine if there had been any drift in the sensors. Each test was then repeated to ensure consistent results. No discernible difference was detected between test runs. All results were corrected for solid blockage, wake blockage, and streamline curvature based on the techniques presented by Rae and Pope [20].

### III. Flow Characteristics

The nature of low-Reynolds-number LAR aerodynamics results in complex, coupled flow characteristics that cause unconventional loading on a model. To correctly interpret the forces and moments measured by the MLT balance, it is important to obtain some understanding of how the flow behaves to validate the quantitative results. As the prototunnel is not currently equipped with a smoke visualization system, the available options were surface oil or surface tuft testing. As it is desirable to obtain some knowledge of the three-dimensional nature of the flow (specifically, how the rollup of the tip and leading-edge vortices propagates over the suction side of the wing), surface tufts were used as the visualization method. An array of half-inch-long 40-weight nylon string tufts were attached to the top of the wing in rows parallel to the leading edge; in addition, longer strands of string (2 in. long) were attached to the side of the model at the trailing edge to capture the effects of the tip vortex. Images were taken using the Phantom v4.3 high-speed camera mounted directly above the test section.

#### A. Expected Flow Phenomena

It is important to have an understanding of the development of flow phenomena associated with LAR wings at low Reynolds numbers in order to correctly interpret the results from the tuft testing. Mueller and Delaurier [9] and Arena and Mueller [21] have described the development of a leading-edge separation bubble that forms when the laminar boundary layer separates at some location on the top surface of the wing due to the strong adverse pressure gradient. This separation bubble is known to form in the range of Reynolds numbers

typically associated with fixed-wing MAV flight (50,000–200,000). If the transition to turbulence is sufficient to energize the flow by entraining fluid from the surrounding air, the separated flow can reattach to the surface; this results in a recirculation region on the top surface of the wing. This separation bubble is typically observed on airfoil geometries as opposed to flat plate wings; in the latter case, the flow is unable to remain attached around the sharper leading edge, causing a separated shear layer that rolls up into the LEV. Depending upon the flow conditions, including the Reynolds number, angle of attack, and turbulence intensity, this vortex can either cause reattachment at a downstream location (similar to the separation bubble) or give way to a Kelvin–Helmholtz instability and vortex shedding [22,23]. The LEV tends to interact strongly with the developing tip vortices that spill over the sides of the wing due to the pressure differential between the top and bottom surfaces [9,24]. This phenomena is known to have significant effects on the aerodynamic performance of LAR fliers as the small wingspan allows the crossflow from the tip vortex to propagate over most of the wing, thus keeping the flow attached at higher angles of attack [8]. The downwash from the tip vortex tends to force the vortex street produced by the LEV to remain attached to the wing surface, thus enhancing lift at higher angles of attack [25].

For a tapered wing in the same flow regime, the angled leading-edge geometry increases the complexity of the LEV. This has been extensively researched, although typically for the higher sweep angles of a slender delta wing planform in the range of 50–85° [26–29]. The main difference between the LEV on a swept wing as opposed to a rectangular wing is that the former case increases the downstream convection of vorticity due to the spanwise flow along the angled leading edge. In contrast, the latter case experiences little spanwise flow near the leading edge; thus, the predominant mechanism for the release of the vorticity is the shedding of the LEV [25]. As the majority of the available literature is concerned with the visualization of the LEV at higher sweep angles, the formation of a coherent vortical structure in the regimes investigated in this study is a matter of some uncertainty, although experimental results at moderate Reynolds numbers and sweep angles suggest that it is likely that a weak LEV will develop [27,29]. This structure is subject to vortex breakdown at some downstream location over the surface of the wing due mainly to the effects of the adverse pressure gradient, the swirling nature of the vortex core, and the divergence of streamtubes in the core [11]. A decreased swirling magnitude typically requires a smaller positive pressure gradient to cause breakdown; thus, the weak LEV formed by the 35° swept wing is expected to be subject to bursting relatively quickly.

In the context of the surface tuft measurements undertaken in this study, the behavior of the tufts is instructive in determining the degree of separation and the nature and direction of flow on the surface; the trailing-edge tufts are useful for visualizing the development and coherency of the tip vortex at low angles of attack. Observations were made in regard to any periodic nature of the tuft rotation to estimate the coherency of the vortical structures; as a result, each sequence of images spans the time taken for the trailing-edge tufts to complete one rotation. This provides an estimate of the energetics of the tip vortex. Tests were conducted with all of the models with  $AR = 1$  at angles of attack of 0, 10, 20, 30, and 45° at sideslip angles of 0 and 35°. A summary of the results and a selection of images are included to describe the flowfield over the wing.

## B. Tuft Visualization Results

The tuft visualization of the square wing showed the development of tip vortices at angles of attack as low as 5°; these structures were visible due to the rotation of the trailing-edge tufts. This circulation grew in amplitude until an angle of attack of 20°, at which point the interaction between the tip vortex and the recirculation region over the wing caused the rotation to become irregular. This much can be seen in Fig. 3, in which the reversed flow and tip vortex rotation are noticeable near the center of the wing. In addition, the behavior of both the trailing-edge tufts and the surface tufts was observed to be asymmetric about the root chord; this is because the tip vortices themselves become asymmetric at increased angles of attack and swing erratically in a lateral direction [30]. The shedding of these tip vortices into the wake at high angles of attack also produces time-varying side forces that create an unsteady yaw oscillation of the model [25]. The surface tufts are observed to separate from the plate near the leading edge due to the development of the LEV; however, the majority of the tufts on the wing were pressed flush with the surface of the wing due to the induced downwash from the tip vortices. This is a manifestation of the tip vortex interacting with the LEV and keeping the LEV sheet attached to the wing [25]. All of these effects essentially disappeared as the angle of attack was increased to 45°; the trailing-edge tufts did not rotate, no flutter was detected on the surface, and the yawing oscillations ceased. This indicates that, at this high angle of attack, no coherent tip vortices form as the flow is mostly convected downstream. This will cause a rapid deterioration in aerodynamic loading.

The tapered planforms showed the development of a LEV and significant spanwise flow near the leading edge, as seen in Fig. 4 for a taper ratio of 0.25. In addition, the tip vortices were observed to develop at the wingtip and were stronger than the corresponding structures on the square wing. This is because the vorticity generated by the LEV is convected downstream along the leading edge due to the spanwise flow and is fed into the forming tip vortex, increasing its strength [25]; this effect is more pronounced for decreasing taper ratios as a result of the greater spanwise flow. The resulting downwash is effective in keeping most of the surface tufts pressed flush with the wing until angles of attack above 30°, at which point some increased separation was noticeable. At these high angles, the rotation of the trailing-edge tufts becomes more random; results by OI and Gharib suggest that, for these geometries and incidence angles, there is a high likelihood of vortex breakdown [27] that would contribute to the random nature of the flow. Similar to the square wing, once the angle of attack was increased to 45°, the rotation of the trailing-edge tufts is no longer noticeable and the surface tufts no longer give any indication of attached flow on the surface. These changes were observed to occur over an angle-of-attack range of only 2–3°.

The  $\lambda = 0.25$  wing at an angle of attack of 30° and a sideslip angle of 35° is shown in Fig. 5. The flow was seen to exhibit characteristics of both the rectangular and tapered planforms at zero sideslip; this is somewhat unsurprising as the high sideslip angle causes the upwind side of the leading edge to be oriented nearly perpendicular to the flow (similar to the rectangular wing). The downstream leading edge now resembles that of a slender delta wing; in this Reynolds number regime, this is known to result in the formation of a strong LEV, which is expected to break down before reaching the wingtip [28]. This burst vortex helps prevent the formation of a tip vortex on the downstream wingtip, where the trailing-edge tuft is merely directed

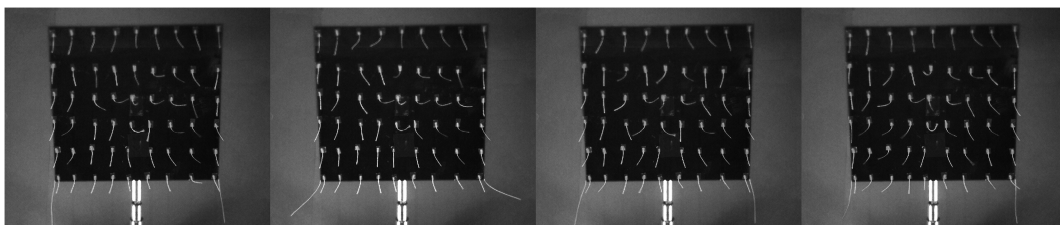


Fig. 3 Surface tuft visualization for a square plate with  $c = 6$  in. at  $Re = 1 \times 10^5$ ,  $\alpha = 30^\circ$ , and  $\beta = 0^\circ$ . Elapsed time of 44 ms. Rotation of the trailing-edge tufts shows increasing influence of the tip vortices. Separation is present at the leading edge and along the centerline, although the tip vortex downwash forces most tufts flush with the surface.

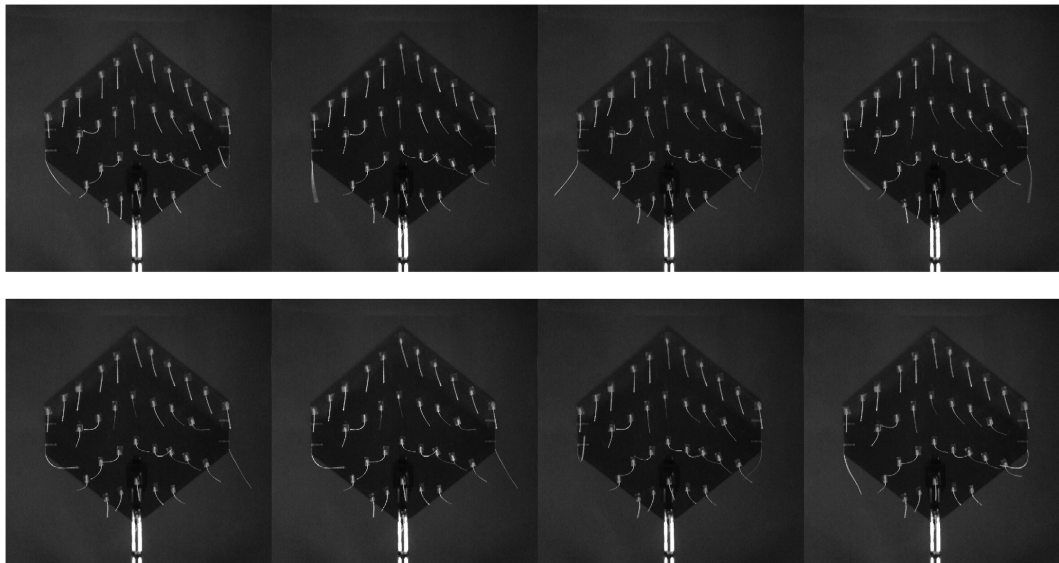


Fig. 4 Surface tuft visualization for a taper ratio of  $\lambda = 0.25$  at  $Re = 1 \times 10^5$ ,  $\alpha = 30^\circ$ , and  $\beta = 0^\circ$ . Elapsed time of 65 ms. Increased reversed flow is noticeable near the trailing edge; however, downwash from the tip vortices keeps most tufts flush with the wing surface. Bias toward root-to-tip flow indicates that some form of LEV is still present. The random nature of the trailing-edge tufts suggests that the LEV has burst before reaching the wingtip.

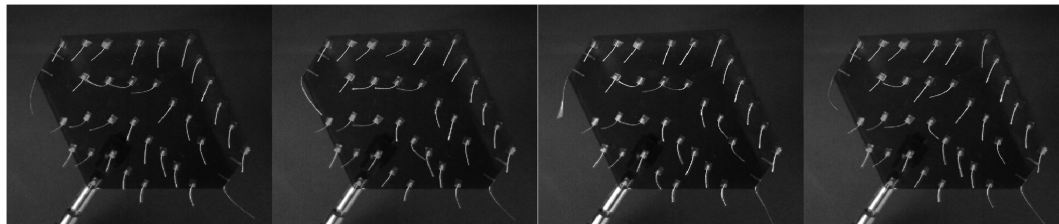


Fig. 5 Surface tuft visualization for a square plate with  $c = 6$  in. at  $Re = 1 \times 10^5$ ,  $\alpha = 30^\circ$ , and  $\beta = 35^\circ$ . Elapsed time of 31 ms. There is more reversed flow noticeable than the  $20^\circ$  case, although the overall behavior of the flow is similar at the higher angle of attack. Spanwise flow on the right leading edge indicates the formation of a LEV, which is slightly weaker than the previous case. The upstream tip vortex behaves similarly to the  $20^\circ$  case.

downstream and displays no rotation. The upstream tip vortex does form, however, and effectively keeps the surface tufts attached over a large surface of the wing. A comparison of Figs. 4 and 5 shows a reduced amount of reversed flow for the wing in sideslip; this is because the upstream leading edge is similar to that of a square wing and promotes increased axial flow that resists separation. Unlike the zero sideslip cases, this flow pattern observed over the wing remains constant up to angles of attack of  $45^\circ$  (the highest angles tested); thus, while the flow over the wing surface is complex, it prevents separation at high angles of attack.

#### IV. Test Results

In this section, a summary of test results are presented to demonstrate the trends associated with the aerodynamics of LAR wings at low Reynolds numbers, the difference that the wing planform geometry has on the loading, and how the effects of lateral perturbations in the form of sideslip angles affect the performance of the model. When relevant, the quantitative results measured using the MLT balance will be referenced to the surface tuft measurements presented in the previous section to describe the flow characteristics.

##### A. System Validation

To validate the performance of the MLT force balance and the MPS, a selection of data from Pelletier and Mueller [7] was chosen for comparison. Despite differences in the experimental setup, such as model material and mounting technique, results were shown to correlate with good accuracy. A test case for comparison at  $Re = 8 \times 10^4$  with  $AR = 3$  is shown in Fig. 6. This particular  $AR$  case was selected as a good validation because the longer span will reduce the effects of tip vortices. As this flow phenomena is a main focus of the investigation, a more conventional verification case was desired. It is

apparent in Fig. 6 that the results agreed well: particularly, the lift curve slope in the linear regime. Other minor variations, such as low angle-of-attack discrepancies in drag and poststall deviation, can be attributed to slight turbulence and experimental setup variations between the two tunnels.

##### B. Varying Aspect Ratio Rectangular Plates

With the accuracy of the measurement and maneuvering system confirmed to be satisfactory, it was possible to progress to more illustrative test cases. As a baseline set of tests, flat plates with  $AR$ s of 0.75, 1, 1.5, and 3 were tested at velocities between 17.1 ft/s (5.2 m/s) and 61.5 ft/s (18.7 m/s), corresponding to freestream chord-based Reynolds numbers of  $5 \times 10^4$ ,  $8 \times 10^4$ , and  $1 \times 10^5$ . Figures 7–9 display the results of the tests. It should be noted that no data are present for  $AR = 3$  in Fig. 9, as the shorter chord would require a higher velocity than the prototunnel can attain to achieve a Reynolds number of  $1 \times 10^5$ . The results of these tests display the same behavior as surmised by Torres and Mueller [8] and depicted in the tuft visualization results in Sec. IV; a decreased  $AR$  allows the crossflow produced by the tip vortices to propagate further along the wing and create a nonlinear increase in lift at high angles of attack.

Another point of interest in the data is the drag polar in the stall regime, which also displays nonintuitive results that were not discussed by Torres and Mueller [8]. Although not all test cases could be taken completely to stall behavior due to geometric constraints within the tunnel, those that did stall (as determined by the location of  $C_{L_{max}}$ ) recorded a decrease in drag as angle of attack was increased. This can best be seen in Fig. 9b, where both the  $AR = 1$  and  $AR = 1.5$  cases stall and then experience a deficit in drag for several data points; in the  $AR = 1$  case, the drag coefficient does not recover to its maximum value of 1.61 measured at an angle of attack of  $43^\circ$ .

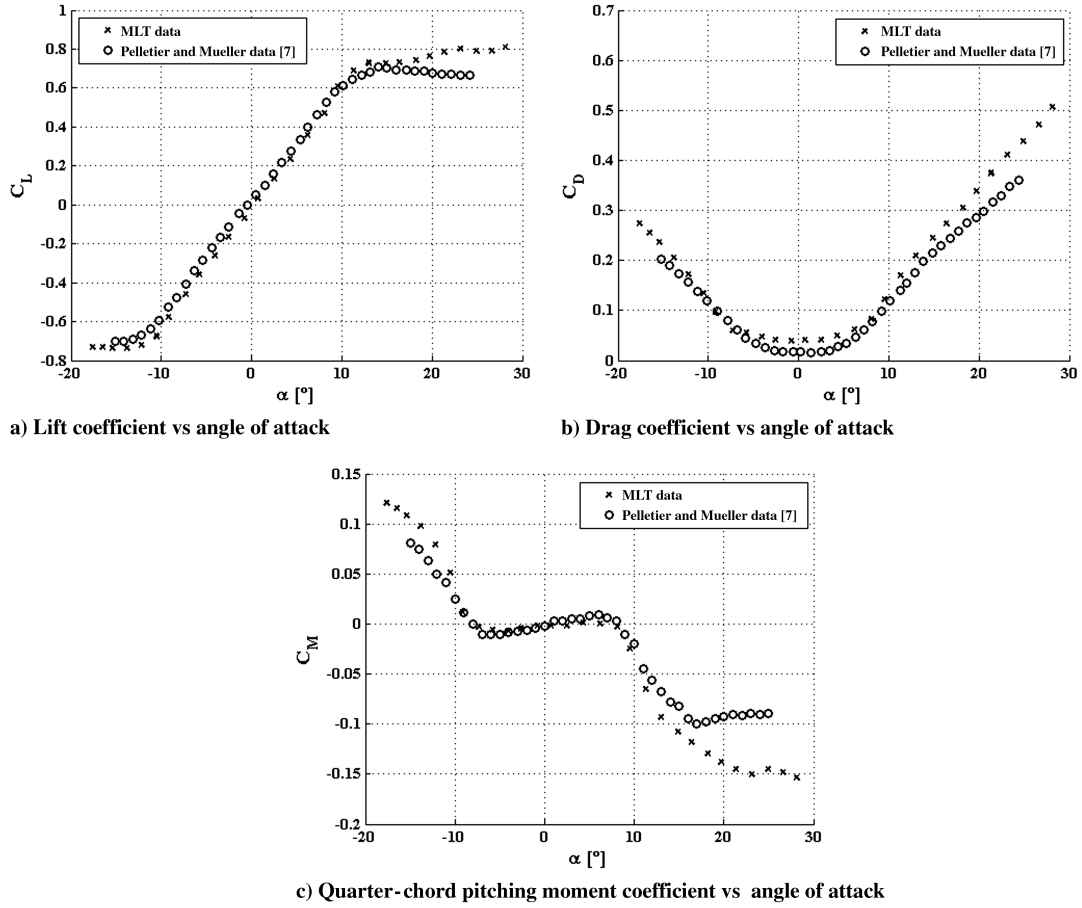


Fig. 6 System validation: comparison with results from Pelletier and Mueller [7] for a rectangular flat plate platform with  $AR = 3$  at  $Re = 8 \times 10^4$ .

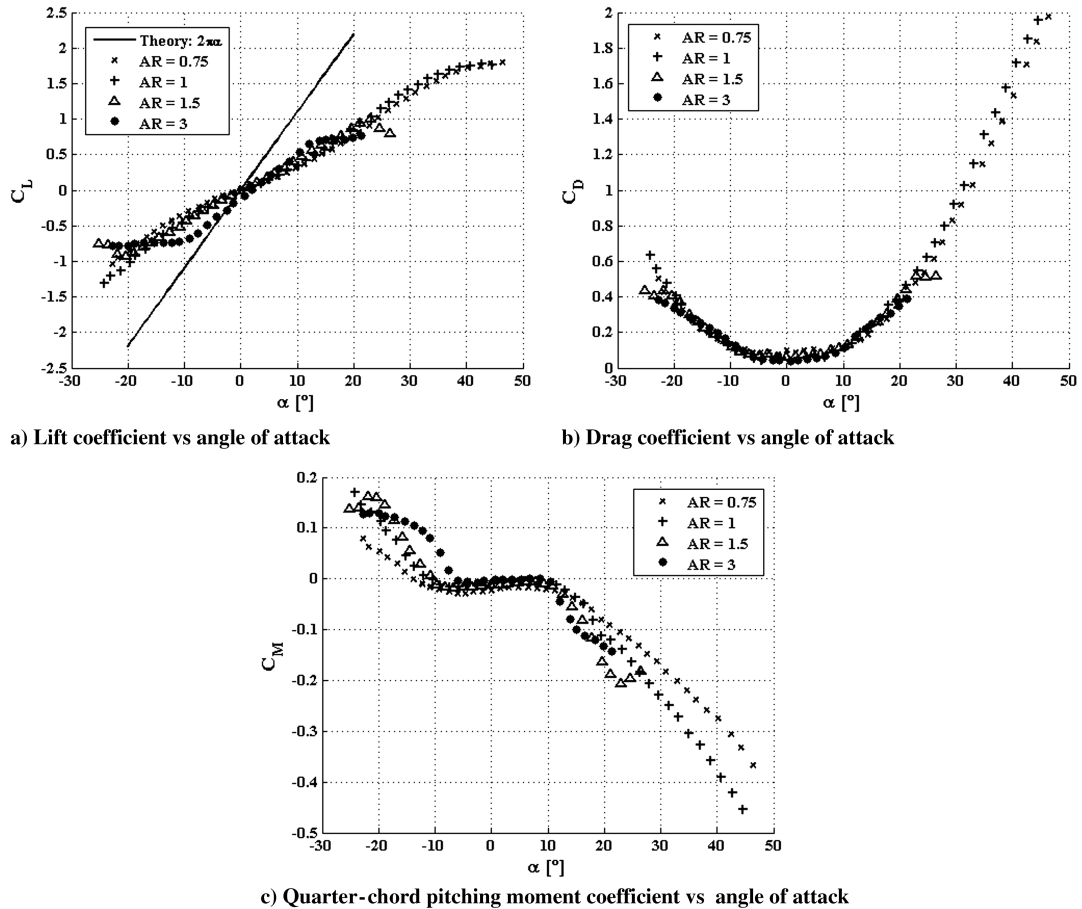


Fig. 7 Aerodynamic loads on rectangular flat plate platforms with varying  $AR$  at  $Re = 5 \times 10^4$ .

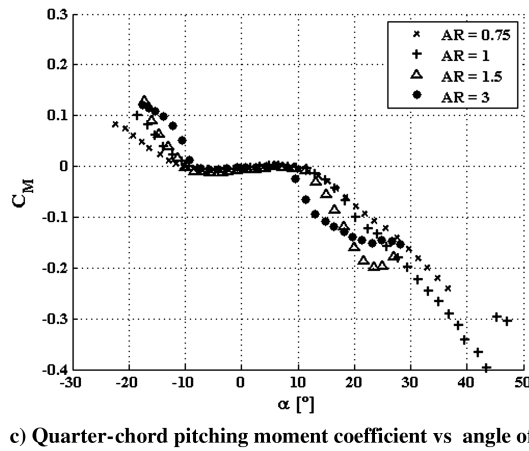
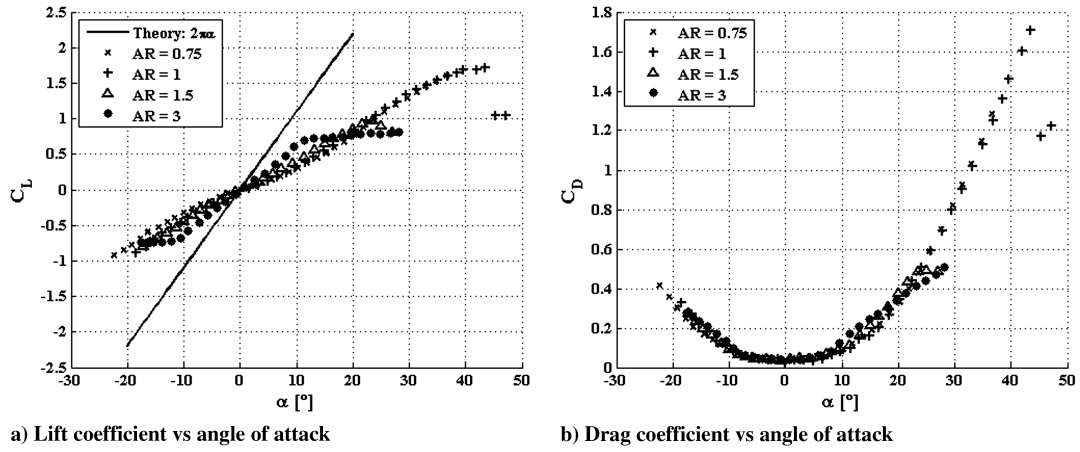


Fig. 8 Aerodynamic loads on rectangular flat plate planforms with varying AR at  $Re = 8 \times 10^4$ .

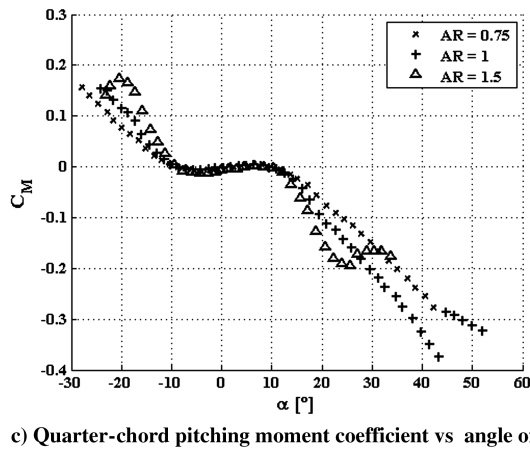
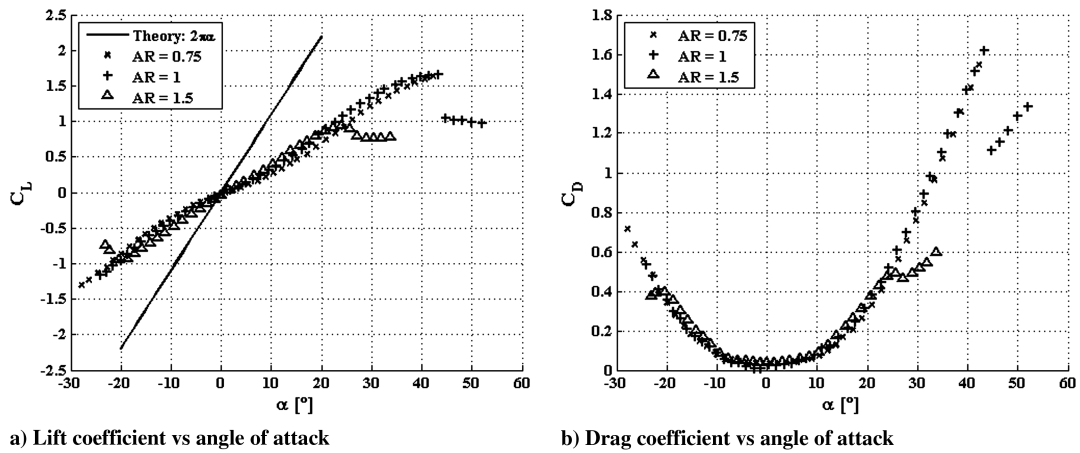


Fig. 9 Aerodynamic loads on rectangular flat plate planforms with varying AR at  $Re = 1 \times 10^5$ .

This differs considerably from a conventional drag polar for higher AR wings at higher Reynolds numbers, which will exhibit a continued increase in drag after stall. It is surmised that this behavior, similar to the lift polar, can be attributed to the effects of tip vortices. As the vortices grow in size and strength at higher angles of attack and consume a greater section of the wing, the stall angle is increased to a relatively high angle of attack around  $45^\circ$ . As seen in Sec. III, at this point, the crossflow due to tip vortices dissipates, causing the attached flow over the wing to separate and induce stall. The reduced impact of the tip vortices lowers the induced angle of attack, and thus the induced drag, so that the majority of the drag on the wing is profile drag. It is this reduction in induced drag that causes the drag polar to decrease after the wing stalls. As the angle of attack continues to increase, the resulting increase in drag is due predominantly to profile drag. A final contribution to the reduction in drag is the loss of the low pressure core associated with the tip vortex, which was reported on by Taira and Colonius [25].

This theory of dependence of drag on the presence of tip vortices also helps to explain why the  $AR = 1$  case experiences a larger decrease in  $C_D$  after stall than  $AR = 1.5$ . The smaller AR relies on nonlinear lift from the tip vortices to reach its high stall angle, and when the flow does detach around  $43^\circ$ , there is a greater reduction in induced drag than when the larger AR stalls at  $25^\circ$ . It should also be noted that, although at this high angle of attack the incidence geometry of the wing begins to resemble that of a bluff body, no unsteady effects on the loading caused by asymmetric vortex shedding were measured. The Strouhal number of vortex shedding based on the freestream velocity and projected frontal height of the model is expected to be 0.2 for the range of Reynolds numbers in this investigation [22,23]; this corresponds to an expected shedding frequency in the order of 30 Hz. As the measured experimental data are the mean value of a 1 s sample time, these unsteady effects were averaged out to obtain the mean loads.

It is clear from Figs. 7–9 that AR is by far the most important factor in measuring the effects of tip vortices. Although freestream velocity (and thus Reynolds number) does play a role in the loading, only small variations are present for a given AR between Reynolds numbers of  $5 \times 10^4$  and  $1 \times 10^5$ . As the geometric effects of the wing are so prevalent in the results, the next logical step is examining a tapered model to examine how further changes to the wing shape affect the aerodynamics. As the results from different Reynolds numbers were not significantly different, only data from  $Re = 1 \times 10^5$  will be presented.

### C. Varying Taper Ratios for a Flat Plate with Aspect Ratio of Unity

A set of four plates with taper ratios of  $\lambda = 0.25, 0.5, 0.75$ , and 1 were fabricated for testing, with the taper ratio defined as  $\lambda = c_{tip}/c_{root}$ . For this test, the AR was held constant at 1 as the previous data indicated that this would allow the best stall characterization. All models were fabricated with a root chord of 6 in. so that the freestream tunnel velocity (and thus the turbulence intensity) would be constant for each test. Models were tested at a freestream velocity of 38.1 ft/s (11.6 m/s), corresponding to a Reynolds number of  $1 \times 10^5$ . The measured loads normalized by the dynamic pressure, planform area, and root chord of the wing are shown in Fig. 10.

As the models tested were of  $AR = 1$ , each was successfully taken to stall. Figure 10a shows that the stall angle for the different taper ratio models was mostly unchanged and remained around  $42^\circ$  for each wing. The biggest difference between the models is the greater lift coefficient of the rectangular plate: somewhat unsurprising given the much larger lifting surface of the  $\lambda = 1$  case and the increased impact of the reversed flow over the tapered trailing edge seen in the tuft visualization. The maximum lift coefficients of the cases  $\lambda = 0.75$  and  $\lambda = 0.5$  are correspondingly lower; however, the  $\lambda = 0.25$  model has a higher  $C_{L_{max}}$  than the other tapered models despite its

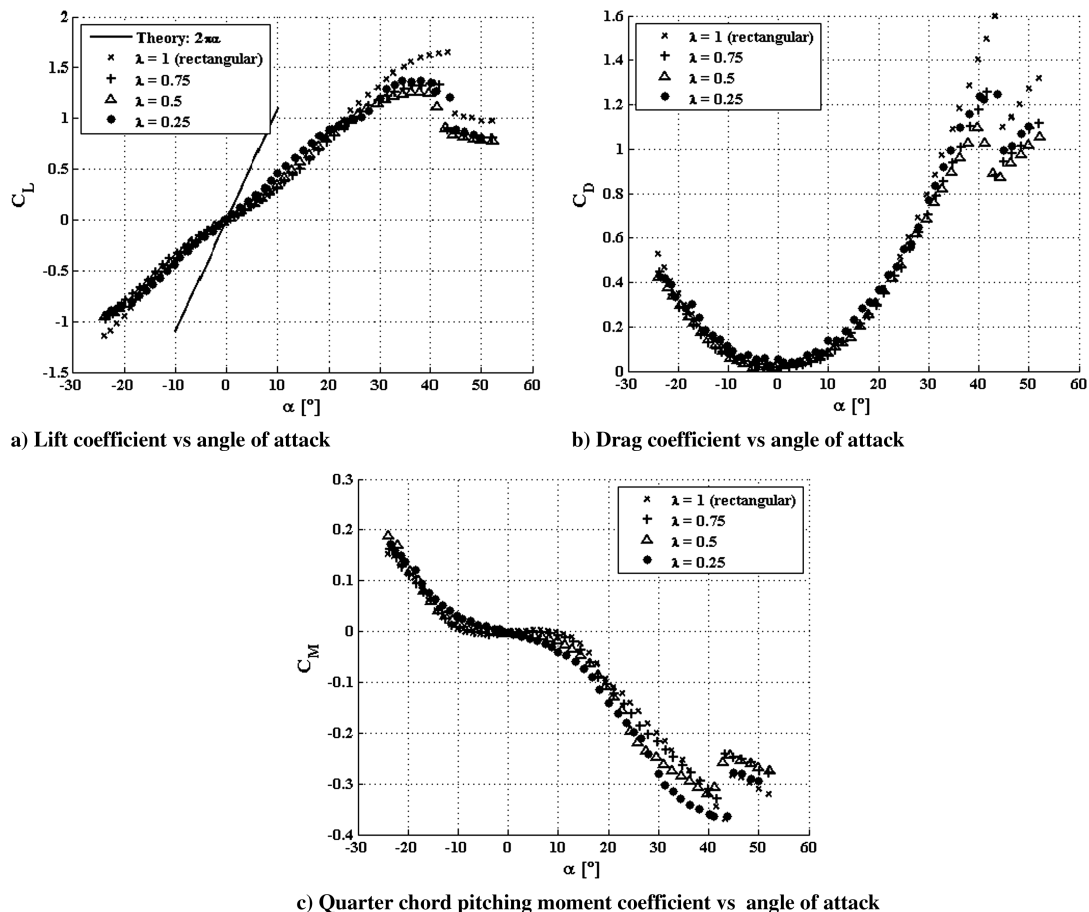


Fig. 10 Aerodynamic loads on flat plate planforms with varying taper at  $AR = 1$  and  $Re = 1 \times 10^5$ .

smaller lifting surface. At angles of attack greater than  $20^\circ$ , the tip vortex becomes increasingly prevalent and begins to interact with the LEV, although the crossflow effects are less than those felt by the rectangular plate. Still, the interaction allows the flow to remain mostly attached at higher angles of attack. This much was seen from the tuft visualization in Sec. III. From Fig. 10a, it is clear that the interactive effects of the LEV and the tip vortices at low taper ratios and high sideslip angles result in a beneficial increase in  $C_{L_{max}}$ .

#### D. Effects of Sideslip on Tapered Wings

It is clear from the test results of the previous sections that LAR fliers can be greatly affected by crossflow over the surface of the wing, particularly at high angles of attack. To this point, only the zero sideslip case has been considered; while this is a useful study, the ultimate goal of this research is to develop a better understanding of low-Reynolds-number aerodynamics to facilitate MAV design. These aircraft have been observed to be highly susceptible to lateral perturbations such as gusts; thus, it is also important to investigate how a lateral component of freestream velocity affects the loading on the models. The MPS was designed to combine degrees of freedom such as sideslip and pitch, allowing these effects to be accurately tested. For these tests, the model was rotated to sideslip angles of  $\beta = 10, 20,$  and  $35^\circ$  and was then pitched through the same range of angles of attack tested at  $\beta = 0^\circ$ . The tunnel velocity was kept at 38.1 ft/s to simulate a condition in which a MAV is laterally perturbed from its freestream flight velocity (for example, if a gust instantaneously hit the tail surfaces) and now continues moving forward at a newly induced sideslip angle. In essence,  $\beta = 0^\circ$  is considered to be a "cruise" flight condition. Results for the different taper ratios are shown in Figs. 11–13.

The results of testing the tapered planforms at various sideslip angles show the decrease in aerodynamic performance as the wing yaws. From Fig. 11, one can consider the  $\beta = 0^\circ$  case a baseline for comparing the different yaw angles of the various taper ratios. It is

clear that increasing the sideslip angle causes a decrease in lift curve slope. As described in Sec. III, the flow over a tapered wing in sideslip is complex by nature, with the downwind half of the wing mostly affected by the LEV and the upwind half more affected by conventional flow over the leading edge and the propagation of the tip vortex. The increasingly interactive flow reduces the lift curve slope as the sideslip angle increases, as seen in Fig. 11, although no sharp stalls or increases in nonlinear lift are apparent at high values of  $\beta$ . The combination of conventional flow, tip vortex propagation, and LEV spanwise flow interact significantly but result in similar flow conditions at angles of attack greater than  $20^\circ$ ; thus, there is no drastic stall behavior or nonlinear lift augmentation in the case of the case of the smaller taper ratios at high sideslip angles.

While the decrease in lift and drag do not individually degrade the performance of the aircraft (in the case of the drag polar, reduced drag could even be seen to be a fortunate consequence of a major gust), the disadvantage is clear from observing the pitching moment about the quarter-chord. Figure 13d shows a significant decrease in the magnitude of the pitching moment as the sideslip angle increases. At angles of attack as low as  $15^\circ$  (a reasonable cruise angle for a MAV), the  $\beta = 35^\circ$  case begins to diverge from the baseline reference. In terms of conventional aircraft stability, this represents a decrease in the derivative  $C_{M,\alpha}$  or a reduced ability to recover from pitch perturbations [31]. Physically, this indicates that a LAR flier perturbed from a nominal cruise condition into a sideslip angle quickly loses its ability to maintain a stable angle of attack. A final point to note in Fig. 13 is the complete lack of a zero  $C_{M,\alpha}$  derivative at small angles of attack but increasing sideslip angles. In terms of aircraft performance, this indicates that the static longitudinal stability of the wing is degraded, as the location of the aerodynamic center is not constant even at low angles of attack [32]. A MAV flying in a gusty environment is thus challenged by cross-coupled effects initiated by lateral perturbations and must be longitudinally stable enough to withstand side gusts.

An interesting point to note is some of the similarities between the incident geometries of wings with different taper and sideslip angles:

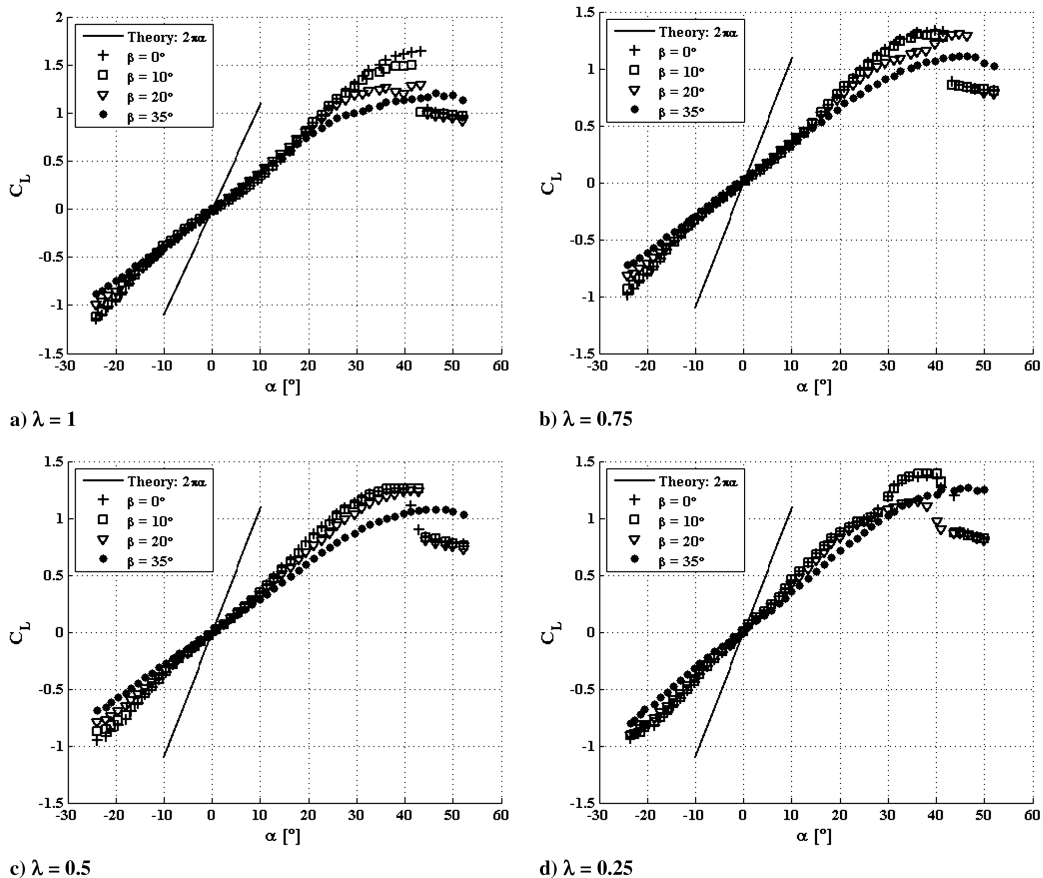


Fig. 11 Lift coefficient of rectangular and tapered flat plates in sideslip at  $AR = 1$  and  $Re = 1 \times 10^5$ .

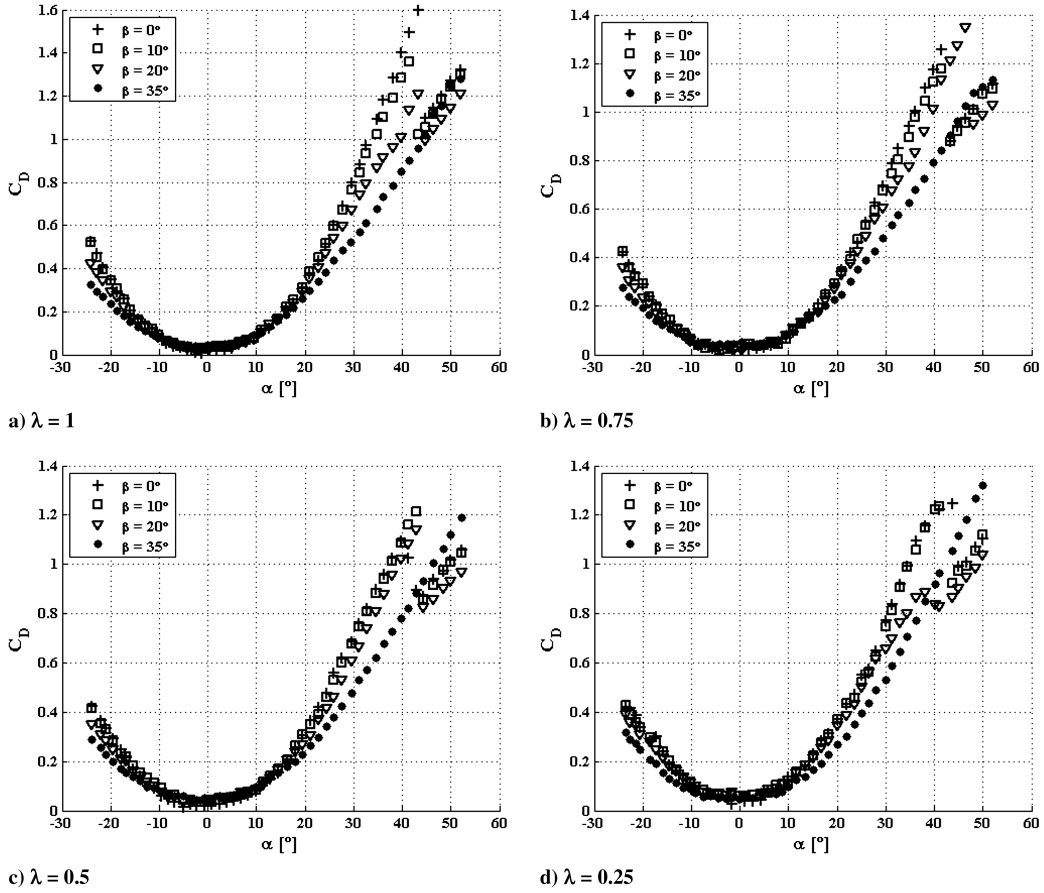


Fig. 12 Drag coefficient of rectangular and tapered flat plates in sideslip at  $AR = 1$  and  $Re = 1 \times 10^5$ .

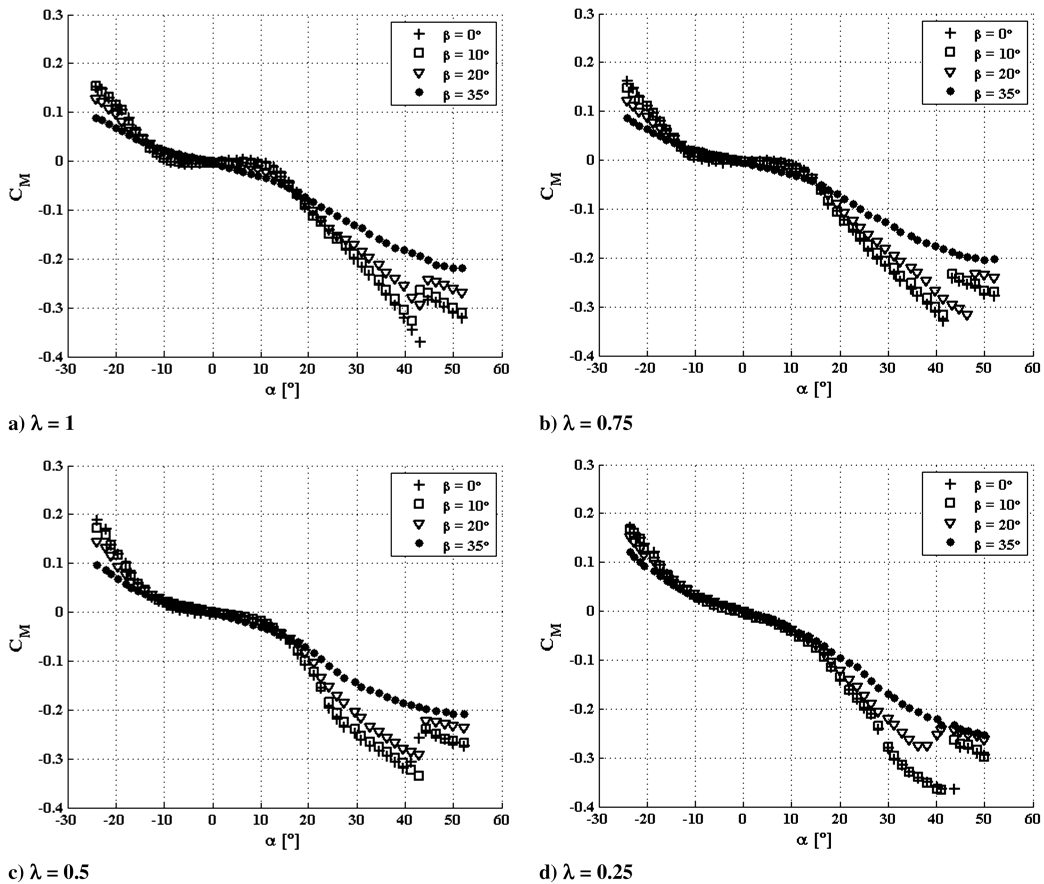


Fig. 13 Quarter-chord pitching moment coefficient of rectangular and tapered flat plates in sideslip at  $AR = 1$  and  $Re = 1 \times 10^5$ .

for example, the  $\lambda = 0.25$  model (which is approximately square, as seen in Table 2) at a sideslip angle of  $\beta = 35^\circ$  presents its upwind leading edge nearly perpendicular to the freestream flow, similar to the rectangular wing at  $\beta = 0^\circ$ . This could potentially lead to similar lift polars; however, examining Figs. 11a and 11d indicates that both  $C_{L_{\max}}$  and  $\alpha_{\text{stall}}$  are different. This is because the smaller taper ratio plate has a much smaller surface area than the  $\lambda = 1$  model in addition to a partially tapered trailing edge that allows increased reversed flow. This causes the reduction in lift coefficient. The  $\lambda = 0.25$  case does show a higher stall angle as the slight effective taper in the leading edge allows some stabilizing spanwise flow to develop that prevents the drastic separation seen for the rectangular wing.

### E. Effects of Winglets on Tapered Wings

Many of the phenomena described thus far can be explained by the influence of tip vortices, which have been seen to contribute to lift, drag, and pitching moment coefficients. It is instructive, therefore, to attempt to reduce the impact of the crossflow over the top surface of the wing with the addition of winglets to the tips of the test models. Some computational work has been done by Viieru et al. [33] to investigate the effects of winglet additions to a MAV wing at lower angles of attack (6 and  $15^\circ$ ), with results indicating an increase of lift and drag as well as the lift-to-drag ratio. It is desirable to test these configurations at higher angles of attack to capture the more dominant effects of the tip vortices. In addition, tests were run for the same taper ratios and sideslip angles used to produce Figs. 11–13. Winglets were tested in three configurations (mounted above the wing, centered on the wing, and mounted below the wing) to determine which setup had the most effect on the crossflow. Again, tests were run at  $Re = 1 \times 10^5$  and a corresponding freestream velocity of 38.1 ft/s.

Selected results from taper ratios of  $\lambda = 0.75$  and  $\lambda = 0.25$  are shown in Figs. 14–19. These plots help to illustrate the significance

of the tip vortices on aerodynamic performance. The general results from Viieru et al. are confirmed; both the lift coefficient and the drag coefficient increase at lower angles of attack and at all sideslip angles [33]. This is to be expected as the winglets help to minimize the reduction in induced angle of attack and thus generate more lift. The increase in drag as the model yaws is obvious as the winglets present a greater impedance to the flow and cause the profile drag to increase significantly. Both coefficients are at a maximum with the winglets below the wing and a minimum with above-wing configuration. An interesting point to note in Fig. 14d is that the lift coefficient is nonzero at an angle of attack of  $\alpha = 0^\circ$  for the centered and below-wing configurations. At this high lateral perturbation, with some surface area of the winglet below the wing, a high enough blockage is created that the pressure below the wing is greatly increased and causes an increase of lift even at small angles of attack. While it seems that this could potentially provide a benefit in MAV design, the corresponding drag polar indicates that, in this same range of angles of attack, the drag coefficient increases from 0.05 to almost 0.4, negating the performance benefit in lift. In addition, the same nonzero  $C_{M,\alpha}$  derivative at low angles of attack as seen in Fig. 13 indicates that the location of the aerodynamic center is not constant for any of the angles tested.

Perhaps the most significant results shown in Fig. 14 are the drastic reduction in nonlinear effects for the centered and below-wing configurations. Only the above-wing geometry displays the recovery in lift coefficient after stall attributed to the contribution of crossflow from the tip vortices. Considering the drag polars in Fig. 15, only the case with the above-wing configuration demonstrates any significant nonlinear effects. This is a direct result of minimizing the effects of tip vortices as their development is impeded by the presence of the winglets below the wing; thus, they cannot contribute to the  $C_L$  recovery. It is clear from Fig. 14 that attempting to block the crossflow by using an above-wing configuration is less effective in reducing the effects of the tip vortex as nonlinear lifting effects remain prevalent at  $\beta = 35^\circ$ .

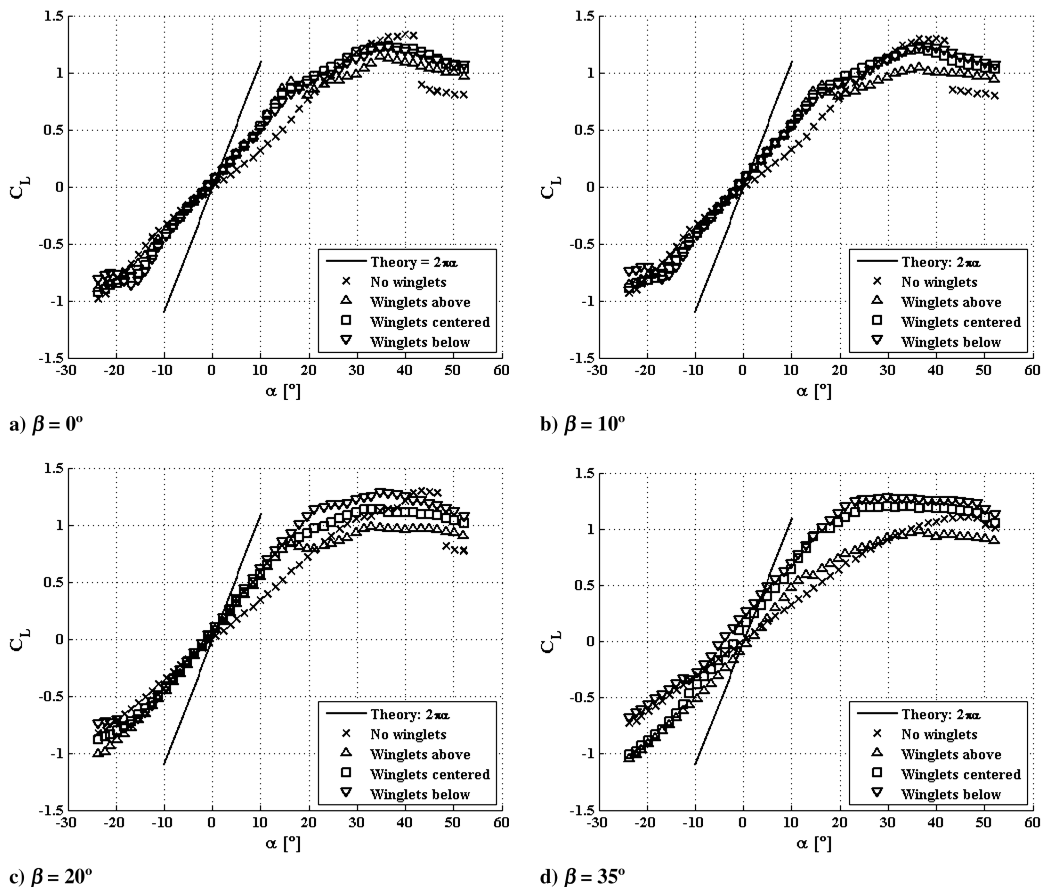


Fig. 14 Lift coefficient vs angle of attack for a tapered plate ( $\lambda = 0.75$ ) at various sideslip angles and winglet configurations with  $AR = 1$  and  $Re = 1 \times 10^5$ .

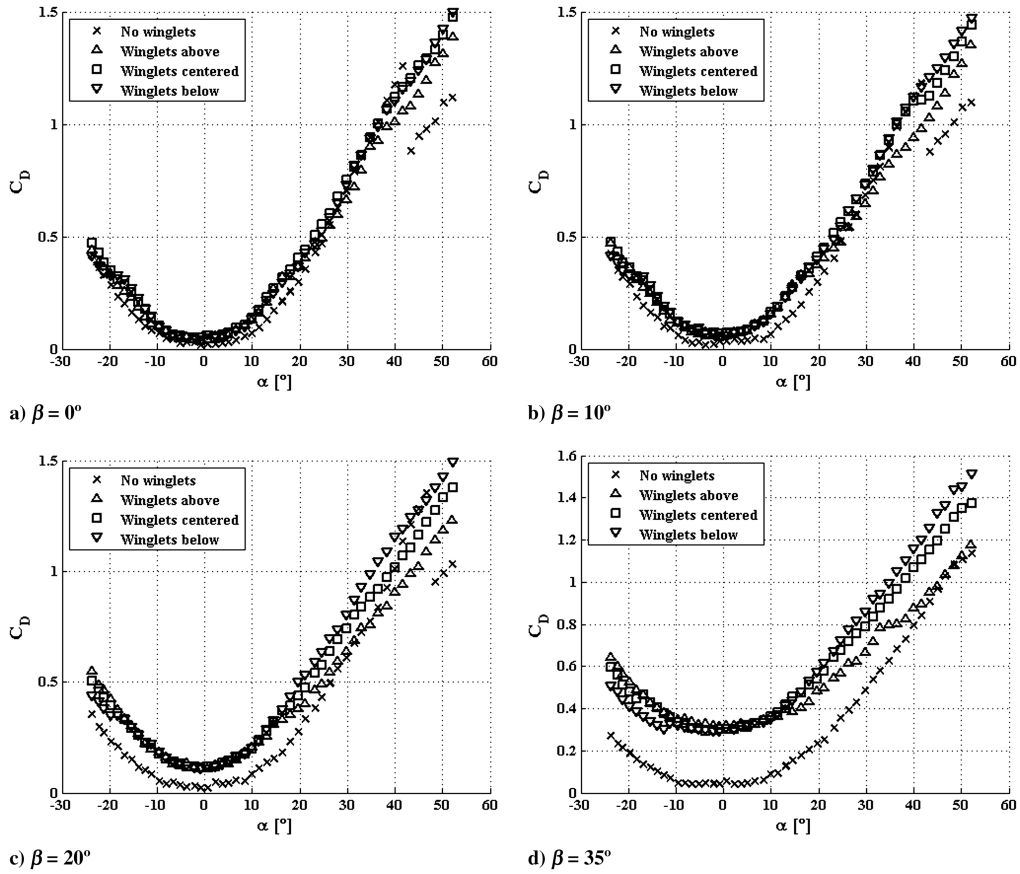


Fig. 15 Drag coefficient vs angle of attack for a tapered plate ( $\lambda = 0.75$ ) at various sideslip angles and winglet configurations with  $AR = 1$  and  $Re = 1 \times 10^5$ .

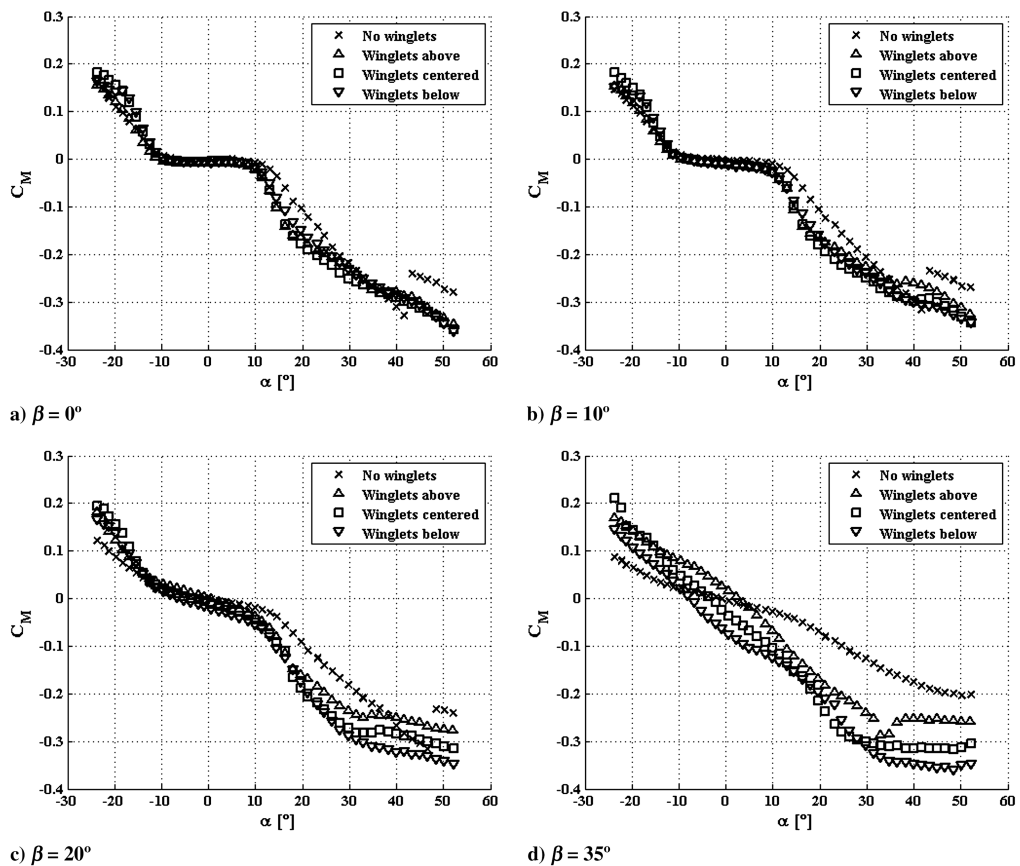


Fig. 16 Quarter-chord pitching moment coefficient vs angle of attack for a tapered plate ( $\lambda = 0.75$ ) at various sideslip angles and winglet configurations with  $AR = 1$  and  $Re = 1 \times 10^5$ .

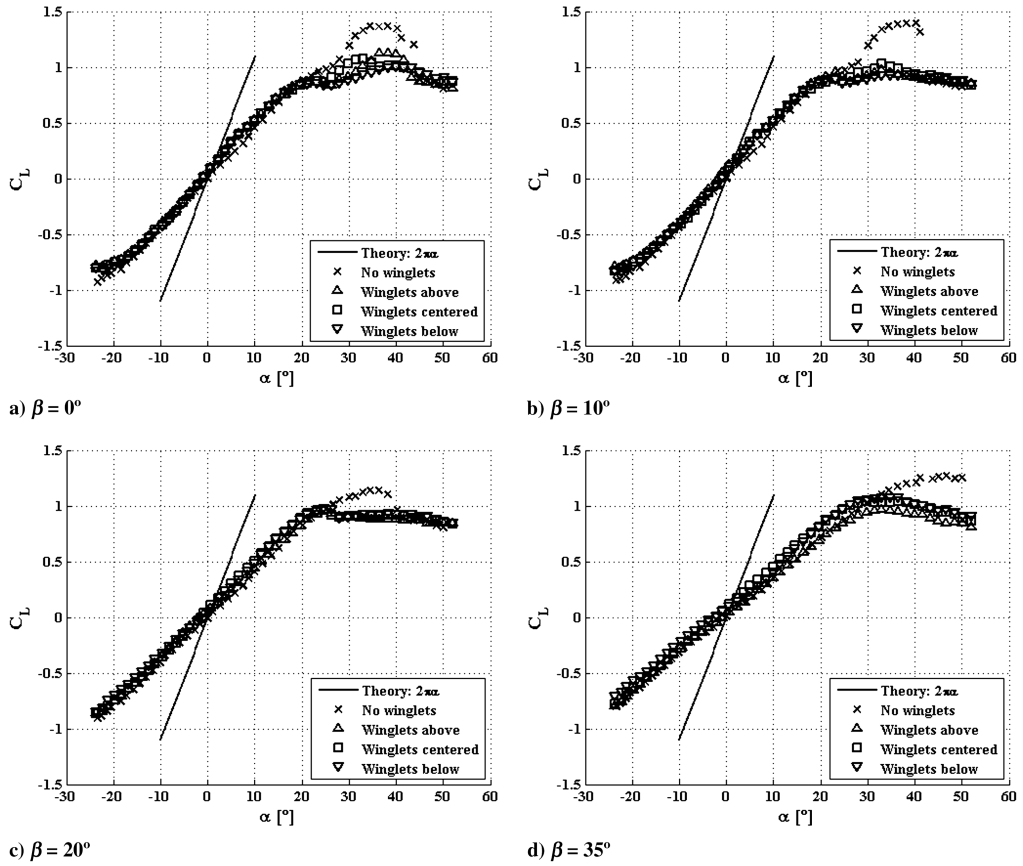


Fig. 17 Lift coefficient vs angle of attack for a tapered plate ( $\lambda = 0.25$ ) at various sideslip angles and winglet configurations with  $AR = 1$  and  $Re = 1 \times 10^5$ .

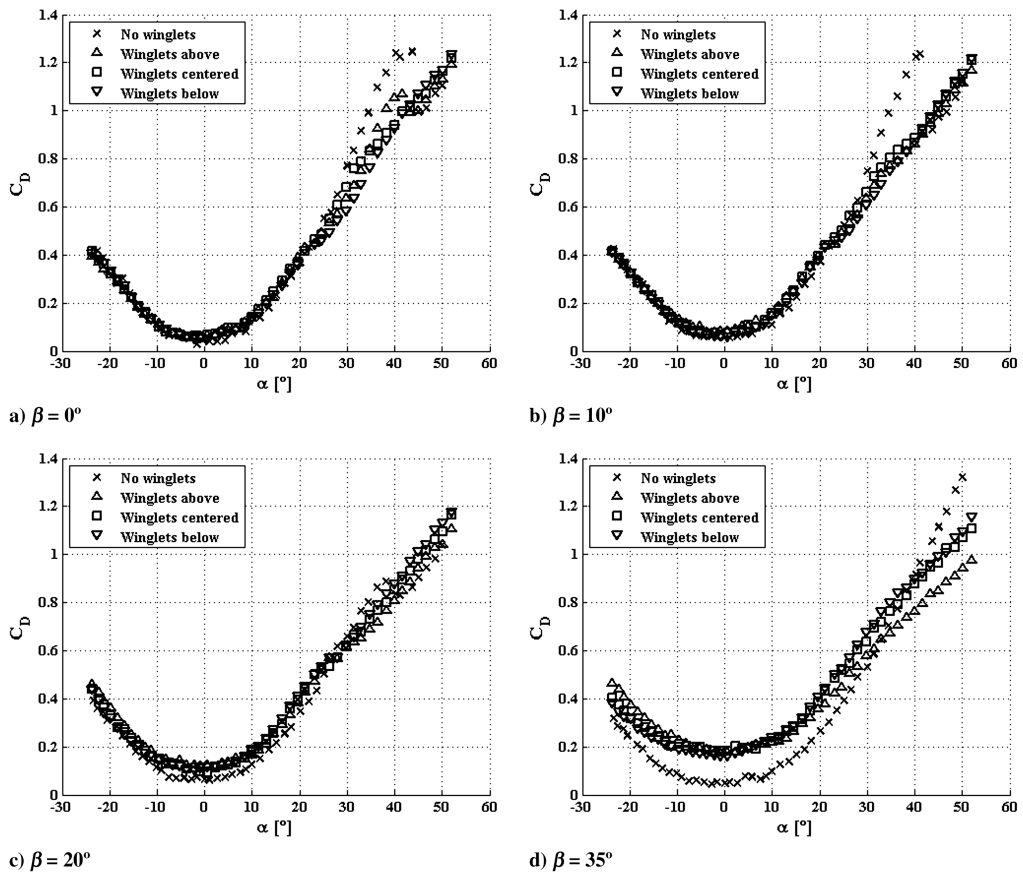


Fig. 18 Drag coefficient vs angle of attack for a tapered plate ( $\lambda = 0.25$ ) at various sideslip angles and winglet configurations with  $AR = 1$  and  $Re = 1 \times 10^5$ .

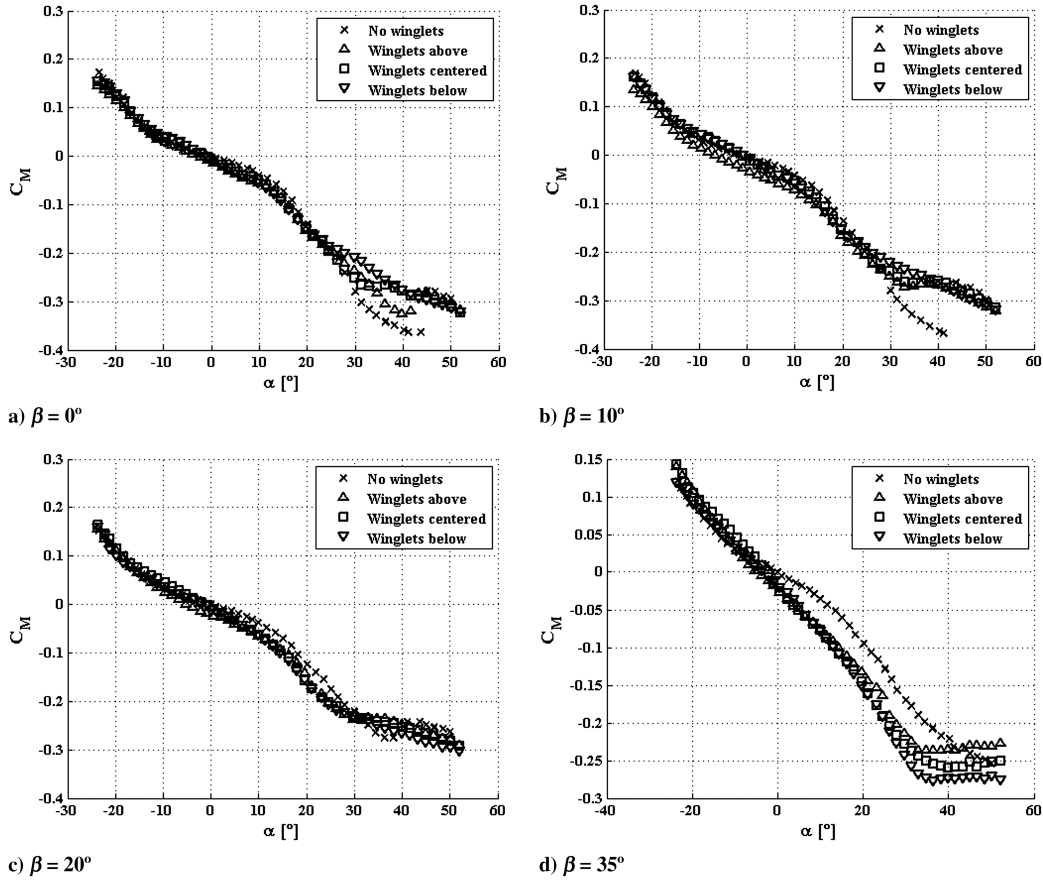


Fig. 19 Quarter-chord pitching moment coefficient vs angle of attack for a tapered plate ( $\lambda = 0.25$ ) at various sideslip angles and winglet configurations with  $AR = 1$  and  $Re = 1 \times 10^5$ .

It is believed that the effects from the winglets are significantly reduced with an increase in sideslip angle as the freestream flow simply convects the vortex downstream. While the linear relationship between angle of attack and loading is beneficial for simplifying aerodynamic analysis, it must also be noted that the decrease in  $\alpha_{\text{stall}}$  and  $C_{L_{\text{max}}}$  as well as the significant increase in  $C_D$  indicate a deterioration in flight conditions with the reduced crossflow.

For the lower taper ratio of  $\lambda = 0.25$ , the first observation from Figs. 17–19 is that the winglet configuration has significantly less influence than the  $\lambda = 0.75$  case, as the results for the three geometries are very similar. This is to be expected, as the smaller winglet surface area has less effect on the loading; however, it is clear that the nonlinear effects are essentially eliminated at all sideslip angles, as seen in Fig. 17. As the angle of attack increases and the wing begins to stall, even the smaller winglet geometry is sufficient to prevent the lift increase at high angles of attack. The results for all sideslip conditions show that lift curve slopes are nearly identical to the no-winglets case until approximately  $\alpha = 25^\circ$  where the effects of tip vortices, if not tampered with, allow the wing to produce an increased  $\alpha_{\text{stall}}$  and  $C_{L_{\text{max}}}$ . Interestingly, the cases with the winglets actually produce lower drag at these high angles of attack, as the induced drag, which is significant for the more dominant tip vortices, is reduced. Figure 18d indicates that the winglets do have the effect of increasing the drag coefficient at low angles of attack for the same reason as previously stated.

From these results, it is apparent that the effects of tip vortices are beneficial for LAR low-Reynolds-number wings, particularly at increasing sideslip angles. Although the lift can in some cases be increased at low angles of attack by altering the wing geometry to reduce the impact of tip vortices, this also results in decreased  $\alpha_{\text{stall}}$  and significantly increased drag at higher sideslip angles. As MAVs are known to be susceptible to lateral perturbations, it is vital to maintain good performance as the aircraft yaws. At increased taper ratios, the adverse effects of the winglet geometry on  $\alpha_{\text{stall}}$  and drag

are noticeable at higher sideslip angles (despite the reduction in induced drag), although the desired lift increase at lower angles of attack is eliminated.

## V. Conclusions

To investigate the influence of Reynolds numbers, AR and sideslip angle on the aerodynamic performance of LAR wings, a series of wind-tunnel tests were conducted on rectangular and tapered flat plate models at Reynolds numbers between  $5 \times 10^4$  and  $1 \times 10^5$ . Surface tuft visualization was conducted to determine the flow characteristics at various geometries and incidence angles. These results indicated that the development of tip vortices at increased angles of attack, coupled with the formation of a LEV, created a complex and coupled flow over the wing that nevertheless maintained attached flow on the top surface of the wing. As a result, stall was delayed until almost  $45^\circ$ ,  $C_{L_{\text{max}}}$  increased to over 1.5, and considerable nonlinear behavior was noticed at higher angles of attack; this much was reported in great detail by Torres and Mueller [8], and the lift coefficient results from this study confirm many of their observations.

Further investigation indicates that these same geometries experience an unexpected decrease in drag coefficient after the onset of stall. It is surmised that this can be attributed to the separation of the tip vortices at the high stall angles associated with LAR wings at low Reynolds numbers. Once the wing stalls, the pressure deficit in the wake is so significant that the crossflow over the top surface of the wing is greatly reduced. As a result, the induced angle of attack and the induced drag rapidly decrease and the majority of the remaining drag is attributed to the profile of the model in the test section. These results were confirmed by the surface tuft visualization.

The contributions of the crossflow were also studied for tapered geometries at various sideslip angles. Tests at a sideslip angle of  $\beta = 0^\circ$  indicated that a smaller taper ratio (that is, a shorter tip chord)

could produce a greater  $C_{L_{max}}$  than larger values of  $\lambda$ ; however, this corresponds to an increased drag coefficient at higher angles of attack. Tuft visualization results indicated that this was predominantly due to the strength of the tip vortices, which receive an injection of vorticity during formation due to the spanwise draining of vorticity from the LEV to the tip vortices. Testing the same geometries at sideslip angles of  $\beta = 10^\circ, 20^\circ,$  and  $35^\circ$  indicated that, although there were some differences in lift and drag coefficients, the most relevant aspect to MAV design is the decrease in pitching moment as the sideslip angle increases. The reduced effect of the tip vortices impairs the wing's ability to recover from a potential pitch perturbation, which exposes one of the many complexities associated with designing a stable MAV, as the vehicle is susceptible to cross-coupled disturbance effects not typically considered when modeling conventional aircraft. A study of the effects of winglets on these tapered geometries indicates that displacing the tip vortex flow from the wing greatly reduces the nonlinear behavior of the wing but also results in a general deterioration in flight conditions at increasing angles of attack and sideslip angles: specifically, a reduction in  $\alpha_{stall}$  and an increase in  $C_D$ . From the results of this investigation, it is apparent that, although the effects of MAV-related flow phenomena such as the LEV and the tip vortices are complicated to model or predict, they do have an overall beneficial influence of the aerodynamics of LAR fliers.

## References

- [1] Hundley, R., and Gritton, E., "Future Technology-Driven Revolutions in Military Operations," RAND Corp. Rept. DB-110-ARPA, Santa Monica, CA, 1994.
- [2] Grasmeyer, J., and Keennon, M., "Development of the Black Widow Micro Air Vehicle," 39th AIAA Aerospace Sciences Meeting and Exhibit, Reno, NV, AIAA Paper 2001-0127, 2001.
- [3] Wasak, R., Jenkins, D., and Ifju, P., "Stability and Control Properties of an Aeroelastic Fixed Wing Micro Aerial Vehicle," AIAA Paper 2002-4005, 2001.
- [4] Ifju, P., Jenkins, D., Ettinger, S., Lian, Y., Shyy, W., and Waszak, M., "Flexible-Wing-Based Micro Air Vehicles," 40th Aerospace Sciences Meeting and Exhibit, Reno, NV, AIAA Paper 2002-0705, January 2002.
- [5] Shields, M., and Mohseni, K., "Using Dynamic Wind Tunnel Testing to Assess Micro Aerial Vehicle Stability Characteristics," 40th Fluid Dynamics Conference and Exhibit, Chicago, AIAA Paper 2010-4389, 2010.
- [6] deCroon, G., de Clercq, K., Ruijsink, R., Remes, B., and de Wagter, C., "Design, Aerodynamics and Vision-Based Control of the Delfly," *International Journal of Micro Air Vehicles*, Vol. 1, No. 2, 2009, pp. 71–97. doi:10.1260/175682909789498288
- [7] Pelletier, A., and Mueller, T., "Low Reynolds Number Aerodynamics of Low-Aspect-Ratio, Thin/Flat/Cambered-Plate Wings," *Journal of Aircraft*, Vol. 37, 2000, pp. 825–832. doi:10.2514/2.2676
- [8] Torres, G., and Mueller, T., "Low-Aspect-Ratio Wing Aerodynamics at Low Reynolds Numbers," *AIAA Journal*, Vol. 42, 2004, pp. 865–873. doi:10.2514/1.439
- [9] Mueller, T., and Delaurier, J., "Aerodynamics of Small Vehicles," *Annual Review of Fluid Mechanics*, Vol. 35, 2003, pp. 89–111. doi:10.1146/annurev.fluid.35.101101.161102
- [10] Shyy, W., Lian, Y., Tang, J., Viieru, D., and Liu, H., *Aerodynamics of Low Reynolds Number Fliers*, Cambridge Univ. Press, New York, 2008, pp. 29–35, 44–49, 61–63.
- [11] Hall, M., "Vortex Breakdown," *Annual Review of Fluid Mechanics*, Vol. 4, 1972, pp. 195–218. doi:10.1146/annurev.fl.04.010172.001211
- [12] Lambourne, N., and Bryer, D., "The Bursting of Leading-Edge Vortices: Some Observations and Discussion of the Phenomenon," Aeronautical Research Council Reports and Memoranda 3282, 1962.
- [13] Roadman, J., and Mohseni, K., "Gust Characterization and Generation for Wind Tunnel Testing of Micro Aerial Vehicles," 47th AIAA Aerospace Sciences Meeting, Orlando, FL, AIAA Paper 2009-1290, 2009.
- [14] Roadman, J., and Mohseni, K., "Large Scale Gust Generation for Small Scale Wind Tunnel Testing of Atmospheric Turbulence," 39th AIAA Fluid Dynamics Conference, San Antonio, TX, AIAA Paper 2009-4166, 2009.
- [15] Watkins, S., and Vino, G., "The Turbulent Wind Environment of Birds, Insects and MAVs," 15th Australasian Fluid Mechanics Conference, Univ. of Sydney Paper AFMC00189, Sydney, Australia, Dec. 2004.
- [16] Watkins, S., Milbank, J., Loxton, B., and Vino, G., "The Turbulent Wind Environment of Birds, Insects and MAVs," *Proceedings of the Fifteenth Australasian Fluid Mechanics Conference*, Vol. 44, No. 11, 2006, pp. 2591–2600. doi:10.2514/1.22670
- [17] Williams, D., Quach, V., Kerstens, W., Buntain, S., Tadmor, G., Rowley, C., and Colonius, T., "Low-Reynolds Number Wing Response to an Oscillating Freestream with and Without Feed Forward Control," 47th AIAA Aerospace Sciences Meeting including the New Horizons Forum and Aerospace Exposition, Orlando, FL, AIAA Paper 2009-0143, 2009.
- [18] *Calibration and Use of Internal Strain-Gage Balances with Application to Wind Tunnel Testing (R-091-2003)*, AIAA, Reston, VA, 2003.
- [19] Mueller, T., Pohlen, L., Conigliaro, P., and B. J. Jansen, J., "The Influence of Free-Stream Disturbances on low Reynolds Number Airfoil Experiments," *Experiments in Fluids*, Vol. 1, 1983, pp. 3–14. doi:10.1007/BF00282261
- [20] Rae, W., and Pope, A., *Low-Speed Wind Tunnel Testing*, 2nd ed., Wiley, New York, 1984, pp. 320–327.
- [21] Arena, A., and Mueller, T., "Laminar Separation, Transition, and Turbulent Reattachment Near the Leading Edge of Airfoils," *AIAA Journal*, Vol. 18, No. 7, 1980, pp. 747–753. doi:10.2514/3.50815
- [22] Colonius, T., and Williams, D., "Control of Vortex Shedding on Two- and Three-Dimensional Airfoils," *Philosophical Transactions of the Royal Society, Series A*, Vol. 369, 2011, pp. 1525–1539. doi:10.1098/rsta.2010.0355
- [23] Lam, K., and Leung, M., "Asymmetric Vortex Shedding Flow Past an Inclined Flat Plate at High Incidence," *European Journal of Mechanics B/Fluids*, Vol. 24, 2005, pp. 33–48. doi:10.1016/j.euromechflu.2004.05.004
- [24] Devenport, W., Rife, M., Liapis, S., and Follin, G., "The Structure and Development of a Wing-Tip Vortex," *Journal of Fluid Mechanics*, Vol. 312, 1996, pp. 67–106. doi:10.1017/S0022112096001929
- [25] Taira, K., and Colonius, T., "Three-Dimensional Flows Around Low-Aspect-Ratio Flat-Plate Wings at Low Reynolds Numbers," *Journal of Fluid Mechanics*, Vol. 623, 2009, pp. 187–207. doi:10.1017/S0022112008005314
- [26] Hall, M., "A Theory for the Core of a Leading-Edge Vortex," *Journal of Fluid Mechanics*, Vol. 11, 1961, pp. 209–228. doi:10.1017/S0022112061000470
- [27] Ol, M., and Gharib, M., "Leading-Edge Vortex Structure of Nonslender Delta Wings at Low Reynolds Number," *AIAA Journal*, Vol. 41, No. 1, 2003, pp. 16–26. doi:10.2514/2.1930
- [28] Payne, F., Ng, T., Nelson, R., and Schiff, L., "Visualization and Wake Surveys of Vortical Flow over a Delta Wing," *AIAA Journal*, Vol. 26, No. 2, 1988, pp. 137–143. doi:10.2514/3.9864
- [29] Miaou, J., Kuo, K., Liu, W., Hsieh, S., Chou, J., and Lin, C., "Flow Developments Above 50-Degree Sweep Delta Wings with Different Leading Edge Profiles," *Journal of Aircraft*, Vol. 32, No. 4, 1995, pp. 787–796. doi:10.2514/3.46792
- [30] Tang, J., and Zhu, K., "Numerical and Experimental Study of Flow Structure of Low Aspect Ratio Wing," *Journal of Aircraft*, Vol. 41, 2004, pp. 1196–1201. doi:10.2514/1.5467
- [31] Phillips, W., *Mechanics of Flight*, 2nd ed., Wiley, New York, 2010, p. 382.
- [32] Schmidt, L., *Introduction to Aircraft Flight Dynamics*, AIAA, Reston, VA, 1998, pp. 22–23.
- [33] Viieru, D., Lian, Y., Shyy, W., and Ifju, P., "Investigation of Tip Vortex on Aerodynamic Performance of a Micro Air Vehicle," AIAA Paper 2003-3597, 2003.